Astroparticle Physics 90 (2017) 20–27

Contents lists available at ScienceDirect

Astroparticle Physics

journal homepage: www.elsevier.com/locate/astropartphys

Absolute-energy-scale calibration of ARGO-YBJ for light primaries in multi-TeV region with the Moon shadow observation

B. Bartoli[a,b], P. Bernardini[c,d], X.J. Bi[e], Z. Cao[e], S. Catalanotti[a,b], S.Z. Chen[e], T.L. Chen[f], S.W. Cui[g], B.Z. Dai[h], A. D'Amone[c,d], Danzengluobu[f], I. De Mitri[c,d], B. D'Ettorre Piazzoli[a,b], T. Di Girolamo[a,b], G. Di Sciascio[i], C.F. Feng[j], Zhaoyang Feng[e], Zhenyong Feng[k], Q.B. Gou[e], Y.Q. Guo[e], H.H. He[e], Haibing Hu[f], Hongbo Hu[e], M. Iacovacci[a,b], R. Iuppa[l,m], H.Y. Jia[k], Labaciren[f], H.J. Li[f], C. Liu[e], J. Liu[h], M.Y. Liu[f], H. Lu[e], L.L. Ma[e], X.H. Ma[e], G. Mancarella[c,d], S.M. Mari[n,o], G. Marsella[c,d], S. Mastroianni[b], P. Montini[p], C.C. Ning[f], L. Perrone[c,d], P. Pistilli[n,o], P. Salvini[q], R. Santonico[i,r], P.R. Shen[e], X.D. Sheng[e], F. Shi[e], A. Surdo[d], Y.H. Tan[e], P. Vallania[s,t], S. Vernetto[s,t], C. Vigorito[t,u], H. Wang[e], C.Y. Wu[e], H.R. Wu[e], L. Xue[j], Q.Y. Yang[h], X.C. Yang[h], Z.G. Yao[e], A.F. Yuan[f], M. Zha[e,*], H.M. Zhang[e], L. Zhang[h], X.Y. Zhang[j], Y. Zhang[e], J. Zhao[e], Zhaxiciren[f], Zhaxisangzhu[f], X.X. Zhou[k], F.R. Zhu[k], Q.Q. Zhu[e],
(The ARGO-YBJ collaboration)

[a] Dipartimento di Fisica dell'Università di Napoli "Federico II", Complesso Universitario di Monte Sant'Angelo, via Cinthia, 80126 Napoli, Italy
[b] Istituto Nazionale di Fisica Nucleare, Sezione di Napoli, Complesso Universitario di Monte Sant'Angelo, via Cinthia, 80126 Napoli, Italy
[c] Dipartimento Matematica e Fisica "Ennio De Giorgi", Università del Salento, via per Arnesano, 73100 Lecce, Italy
[d] Istituto Nazionale di Fisica Nucleare, Sezione di Lecce, via per Arnesano, 73100 Lecce, Italy
[e] Key Laboratory of Particle Astrophysics, Institute of High Energy Physics, Chinese Academy of Sciences, P.O. Box 918, 100049 Beijing, PR China
[f] Tibet University, 850000 Lhasa, Xizang, PR China
[g] Hebei Normal University, Shijiazhuang 050016, Hebei, PR China
[h] Yunnan University, 2 North Cuihu Rd., 650091 Kunming, Yunnan, PR China
[i] Istituto Nazionale di Fisica Nucleare, Sezione di Roma Tor Vergata, via della Ricerca Scientifica 1, 00133 Roma, Italy
[j] Shandong University, 250100 Jinan, Shandong, PR China
[k] Southwest Jiaotong University, 610031 Chengdu, Sichuan, PR China
[l] Dipartimento di Fisica dell'Università di Trento, via Sommarive 14, 38123 Povo, Italy
[m] Trento Institute for Fundamental Physics and Applications, via Sommarive 14, 38123 Povo, Italy
[n] Dipartimento di Fisica dell'Università "Roma Tre", via della Vasca Navale 84, 00146 Roma, Italy
[o] Istituto Nazionale di Fisica Nucleare, Sezione di Roma Tre, via della Vasca Navale 84, 00146 Roma, Italy
[p] Dipartimento di Fisica, Sapienza Università di Roma and INFN - Sezione di Roma, Piazzale Aldo Moro 2, 00185 Roma, Italy
[q] Istituto Nazionale di Fisica Nucleare, Sezione di Pavia, via Bassi 6, 27100 Pavia, Italy
[r] Dipartimento di Fisica dell'Università di Roma "Tor Vergata", via della Ricerca Scientifica 1, 00133 Roma, Italy
[s] Osservatorio Astrofisico di Torino dell'Istituto Nazionale di Astrofisica, via P. Giuria 1, 10125 Torino, Italy
[t] Istituto Nazionale di Fisica Nucleare, Sezione di Torino, via P. Giuria 1, 10125 Torino, Italy
[u] Dipartimento di Fisica dell'Università di Torino, via P. Giuria 1, 10125 Torino, Italy

ARTICLE INFO

Article history:
Received 5 November 2016
Revised 13 February 2017
Accepted 14 February 2017
Available online 15 February 2017

ABSTRACT

In 2011 ARGO-YBJ experiment has reported a work to study the absolute rigidity scale of the primary cosmic ray particles based on the Moon's shadow observation. Given the progress in high energy hadronic interaction models with LHC data, in cosmic ray chemical composition measurement and in experimental data accumulation, more updates can be researched. This paper aims to further disentangle the composition dependence in absolute-energy-scale calibration by using specific moon-shadow data which mainly is comprised of light component cosmic rays. Results show that, 17% energy scale error is estimated from

* Corresponding author.
E-mail addresses: min.zha@mail.ihep.ac.cn, zham@mail.ihep.ac.cn (M. Zha).

http://dx.doi.org/10.1016/j.astropartphys.2017.02.004

Keywords:
Cosmic ray
Moon shadow
Energy calibration
Energy spectrum

3 TeV to 50 TeV. To validate the performance of this technique, the light component cosmic ray spectrum in the same energy region is shown.

1. Introduction

Energy calibration has always been a hard task in air shower array experiments. The main issues focus on the fluctuation of air shower development and the hadron interactions in the very forward region which are not well modeled so far. For a long time, at the energy range of as high as 10 TeV–1 PeV, a normalization or a reference point offered by the direct measurement experiments, such as satellite or balloon-borne detectors is usually used. However, constrained by their small geometrical acceptance, the space experiments usually lack statistics in higher energy thus, the connection between the direct measurement and air shower array is not big enough to cover large ranges for a good calibration.

In this paper, we report another idea about energy calibration in high altitude-based air shower arrays using moon shadow at TeV energies. The so-called moon shadow, which is the phenomenon that cosmic rays are hampered by the moon and a deficit in its direction is expected by detectors, was firstly predicted by Clark in 1957 [1]. This effect has been observed by many different experiments such as typical air shower experiment, Cygnus [2], neutrino experiment, IceCube [3] and muon detectors, MINOS [4].

Measurement of the moon shadow may provide many useful information. For example, it can allow us to measure the point spread function of the detector and to estimate the antiproton-proton ratio at TeV energies. In 2012 the ARGO–YBJ experiment has reported [5] lowest upper limits to the antiproton/proton flux ratio in TeV region. This paper focuses on the calibration of the energy response of the detector based on this phenomenon. The position of cosmic-ray Moon shadow depends upon the paths of the particles through the geomagnetic field. Particles with a lower magnetic rigidity will be deflected more than particles with higher rigidity. Roughly speaking the Earth–Moon system can be considered as a spectrometer. In a first approximation, the amount of such displacement in the West–East direction can be calculated as $\frac{1.6^\circ}{E(TeV)/Z}$. For 1 TeV proton, this is of the order of one degree and it turns to be less than 0.1° for cosmic rays energy higher than 10 TeV. Based on this aspect, papers [6,7] presented some works about absolute rigidity scale calibration without cosmic ray primary composition discrimination in the range of rigidity from 3 to 45 (TeV/Z). For example, Tibet air shower experiment [6] reported an energy scale with 12% uncertainty, which was mainly from high energy interaction model and the composition about primary cosmic rays.

Recently considerable progress in cosmic ray composition studies was established, such as the results by ATIC-2, CREAM and PAMELA [8–11]. With the update of high energy hadronic interaction models with the LHC data [12,18] and the lowering of the threshold energy of high altitude air shower arrays, further progresses could be achieved. ARGO-YBJ experiment is a good candidate in this respect. Its 4300 m a.s.l high altitude observation level and nearly full coverage RPC carpet detector allow us to measure cosmic ray moon shadow with a sufficiently low energy threshold and a good angular resolution at multi-TeV region, where the shift effect is sizable. To decrease charge dependence, further selection on primary composition has been applied. All these factors make it possible to measure TeV moon shadow induced by light primary (proton + helium like) particles. Using these dataset and based on MC simulation, a direct link between shower size and primary energy could be established. To validate this calibration energy, the primary proton+helium energy spectrum using the same dataset in the energy between 2 TeV to 50 TeV are also reported.

The paper is organized as follows. The ARGO-YBJ detector is introduced in Section 2. Detailed descriptions of the adopted geomagnetic field and of the used Monte Carlo simulations for air showers and detector response are provided in Section 3, followed by descriptions of the reconstruction procedure, data quality cuts and the details about cosmic ray light component selection in Section 4. The analysis steps to measure the moon shadow induced by light components are reported in Section 5. The energy calibration and the uncertainties in the reconstructed energy are presented in Section 6. In Section 7, two cross checks are presented including the measurement of light component cosmic ray spectrum in the multi-TeV energy range by using the same dataset. Finally, a short conclusion and a future outlook is discussed in Section 8.

2. The ARGO-YBJ detector

The ARGO-YBJ detector is located at the Yang-Ba-Jing Cosmic Ray Observatory (Tibet, China, 30.11°N, 90.53°E) at an altitude of 4300 m a.s.l., corresponding to a vertical atmospheric depth of 606 g/cm^2. It consists of a single layer of Resistive Place Chambers (RPCs), with each RPC (2.8×1.25 m^2) divided into ten basic detection units called pads (55.6×61.8 cm^2). Each pad consists of eight digital readout strips. Twelve RPCs are grouped into a cluster (5.7×7.6 m^2). The central carpet (78×74 m^2) of the detector is fully covered by 130 clusters, whereas 23 clusters form a guard ring surrounding the central carpet for a better shower core reconstruction. The whole array covers a total area of approximately 11,000 m^2. To extend the dynamic range, a charge read-out layer has been implemented by instrumenting each RPC with two large-sized pads called "big-pad" (140×122.5 cm^2 each) [13].

Two independent DAQ systems are implemented in the experiment: the scalar mode and the shower mode. In the current work, only the data from the shower mode are used. In this mode, the arrival time and fired strip pattern of each fired pad are recorded for subsequent geometric reconstruction. The trigger requires 20 fired pads within 420 ns triggering window. This results in a trigger rate is approximately 3.5 kHz [14]. The completed ARGO-YBJ detector has been collecting data since November 2007, and the operation ended in February 2013.

3. Monte Carlo simulation

An extensive Monte Carlo simulation has been carried out to reproduce the geomagnetic field, the air shower cascade development in the atmosphere, and the response in the ARGO-YBJ detector. For the geomagnetic field, the International Geomagnetic Reference Field 11th generation model (IGRF11) [15] is adopted to describe the Earth's field. The CORSIKA-v7350 package [16] is used to simulate the propagation of the extensive air showers through the atmosphere. The low- and high-energy hadronic models used are FLUKA [17] and EPOS-LHC [18], respectively. All shower secondary particles have been tracked down to the energy threshold of 30 MeV for hadrons and muons and 1 MeV for electronmagnetic particles. Five primary groups, including H, He, C-N-O, Mg-Al-Si and Iron, are simulated to account for a realistic chemical composition of primary cosmic rays. The energy spectrum of individual

primary elements is chosen according to the measurements of the CREAM experiment [9,10]. Concerning the detector trigger efficiency, the energy range of the incident cosmic ray is taken from 300 GeV to 1 PeV for proton and helium, and from 1 TeV to 1 PeV for the rest 3 groups. The directions of primary particles are generated along the Moon's orbit, in a sky window of 10° × 10° around the Moon's direction in the local coordinate system, and the maximum zenith angle of moon is set as 40°. To improve the simulation efficiency, a back-tracking method is applied, i.e., the charges of the incident primary particles are reversed, and they are tracked backwards towards the Moon. If the primary cosmic ray hits the Moon, it becomes "moon shadow events".

The named G4argo [19] software based on GEANT4 [20] package is used to simulate the detector response. The measured detector performances, the trigger logic, time resolution, electronic noises, relation between strip and pad multiplicities based on the experimental setting and measurement, are taken into account. To increase the statistics, each simulated air shower event is resampled ten times and the shower core location is randomly sampled within an area of 1500 × 1500 m^2 around the detector center.

4. Data selection and reconstruction

Data collected from Jan. 1, 2008 until Dec. 31, 2012 are used: the number of events is around 5×10^{11}. The shower core position is reconstructed using a fit of the shower lateral distribution to a Nishimura–Kamata–Greisen (NKG) like function. The arrival direction of each shower is estimated assuming a planar shower front in combination with a further conical correction to account for the curvature of the showers, where the conical slope is fixed to 0.03 ns/m.

4.1. Data quality cuts

To keep good reconstruction quality and select well-contained showers, the following cuts are applied for both the simulated samples and the experimental data:

1. Events should have at least 400 fired strips, i.e., $N_{strips} \geq 400$;
2. Events should have a zenith angle $\leq 35°$. This cut is related to the moon orbit and is a compromise between statistical significance and shower attenuation. For larger zenith angle the observation time would increase but the signal of inclined showers at the ground would be strongly reduced. To keep the balance between these two competing factors, $\theta \leq 35°$ is applied;
3. Reconstructed shower cores are located inside the area of 62 × 62 m^2 around the detector center;
4. For every shower event, a variable R_{70} [21], was determined as the radius containing 70% of fired strips, centered around the reconstructed shower core position. By requiring the distance of the reconstructed shower core from the detector center (marked as D_{c2c}) plus R_{70} should be less than 50 m, i.e., $D_{c2c} + R_{70} < 50$ m.

Cut 3 and 4 are introduced to select well reconstructed internal events. The simulation shows that, for proton induced air shower, the contribution ratio from the events located outside of the detector array is less than 4%, and this number is even smaller for other nuclei induced showers. Another purpose of cut 3+4 is to select well contained showers. Simulation results show that the core positions of > 85% selected events are located within a square of 21 m × 21 m. These facts indicates that no obvious difference in the accuracy of the core reconstruction and angular resolution for the selected events was observed. Based on the simulation, the resolution of the shower core has been found to be around 10 m and the angular resolution is better than 0.8° when the number of fired strips, N_{strips}, is greater than 400.

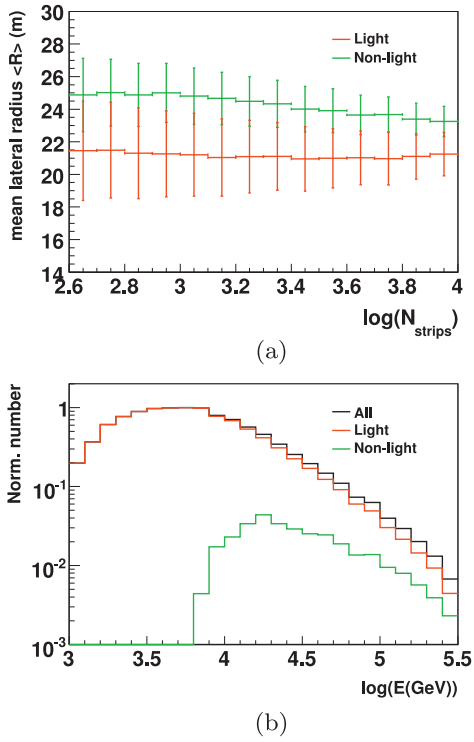

Fig. 1. (a) Mean lateral radius as a function of number of fired strips for light (Proton + Helium) and non-light (C-N-O + Mg-Al-Si + Iron) primaries cosmic ray, where the error bars in y-axis are RMS value of $< R >$, here all quality cuts except composition cut have been used. (b) Energy distribution of survived events after all cuts (1–5) applied. The primary cosmic ray composition is based on CREAM measurement [9,10].

4.2. Heavy component reduction

To reduce the contamination of non-light (C-N-O, Mg-Al-Si and Iron) species, a series of primary composition selection criteria are adopted. Compared to iron showers, for a given energy, showers of light nuclei (proton + Helium) penetrate deeper in the atmosphere. As a consequence, one would expect that the light nuclei showers exhibit a steeper and narrower lateral distribution. A variable, $\langle R \rangle$, named as mean lateral radius, is calculated to select light component showers on the base of this feature [22]. It is defined as: $\langle R \rangle = \frac{\sum(N_i R_i)}{\sum N_i}$, where N_i is the number of strips recorded by the ith fired pad, R_i is the distance from this pad to the shower core. Fig. 1(a) shows the distribution of this variable and its RMS for light/non-light primaries as $N_{strips} < 10^4$, all quality cuts except composition cut (described in late text) have been used. In the calculation, a composition based on the measurements of the CREAM experiment is assumed; Proton and Helium form the light component while C-N-O, Mg-Al-Si and Iron are grouped together as the non-light component. As expected, for internal showers, when the energy increases, the average of $\langle R \rangle$ is quite stable, while the RMS value turns smaller, and $\langle R \rangle$ exhibits a weak dependence on N_{strips}. When cut 5 (named as composition cut), which requires $\langle R \rangle$ less than 24 m, is applied, the non-light CR contribution could be decreased to 2% at energy higher than 1 TeV. Fig. 1(b) shows the energy distribution of survived events. The contribution of events with energies larger than 100 TeV is less than 0.3%.

During the analysis on composition cut, two different selections have been tried. One selection with N_{strips} dependence, such as $\langle R \rangle / m + log10(N_{strips})$, by requiring it less than 26, the simulation shows that no obvious difference existed in comparison with $\langle R \rangle$ value of less than 24 m. Another is to use $\langle R \rangle < 20$ m for

Table 1
Passing ratio of each individual quality cut, the experimental data and MC samples are shown in the bracket.

Cut	Exp. data Passing ratio	MC samples Passing ratio
cut 1+2: $N_{\rm strip} \geq 400$ and $\theta < 35°$	100% (8.3×10^9)	100% (1.1×10^7)
cut 3: $\lvert x_c\rvert \leq 31$ m and $\lvert y_c\rvert \leq 31$ m	31.5%	33.4%
cut 4: $D_{c2c} + R_{70} < 50$ m	46.1%	42.2%
cut 5: $\langle R\rangle < 24$ m	81.9%	80.0%
Cumulative passing ratio	12.0%	11.3%

high multiplicity internal, for example in $N_{strips} > 2000$ internal. It not only further reduced heavy component contamination, but also considerably lowered the significance of the moon shadow. Thus, to keep the balance between heavy component contamination and the statistics, an $\langle R\rangle$ value of less than 24 m is the selected composition cut.

For all selected dataset, the ratio passing through the above individual cuts are shown in Table 1. The difference between experimental data and the simulation samples are treated as an indicator about a systematic uncertainty on the efficiency and will be discussed later in Section 7.2.

5. Analysis of the displacement of moon shadow in West-East direction

5.1. Measurement of moon shadow induced by light component cosmic rays

Light component events survived from cuts 1–5 selections are used to measure the displacement of Moon shadow in West-East direction. Hereafter these data are referred to as Light Moon Data (LMD). To extract the deficit events coming from the direction of the moon, an on-source sky map of size $10° \times 10°$ with grid size of $0.1° \times 0.1°$ around the moon in equatorial coordinate system is constructed. A direct integration method [23] is used to estimate the number of off-source events within each grid cell. To maximize the signal-to-noise ratio for every grid cell, a smooth method that summed up all events in a circular area centered the cell is used to represent its signal strength, while events are weighted by a Gaussian-shape point spread function. The statistical significance of the deficits is given by the formula taken by Li and Ma [24].

Fig. 2 shows the significance distribution in five intervals of strip multiplicity, 400–600, 600–1000, 1000–2000, 2000–3000 and ≥ 3000. Table 2 shows the detailed numbers for the highest significance grid, such as the observed deficit in the grid, the number of off-source events, as well as the optimal angular radius relating the angular resolution and the statistical significance associated with the corresponding radius. As a result of the finite angular size of the lunar disc, the optimal radius does not completely reflect the angular resolution, details are shown in [7]. In the lowest $N_{\rm strips}$ interval, it has an influence at the level of 1%, and the effect is 3% when $N_{\rm strips}$ higher than 2000.

5.2. Displacement of moon shadow in West-East direction

The observed relative deficit event counts around the moon position along the West-East axis (RA direction) is shown in Fig. 3 for the above-mentioned five intervals of strip multiplicity. To obtain this result, the events contained in certain angular band parallel to the East-West axis and centered at the moon position are used. The width of these bands is two times the optimal radius shown in Table 2. The analysis shows different projection range which bring an uncertainty of 2%.

As expected, one can find that the peak position of the deficit counts is gradually shifted to the west with the decreasing of

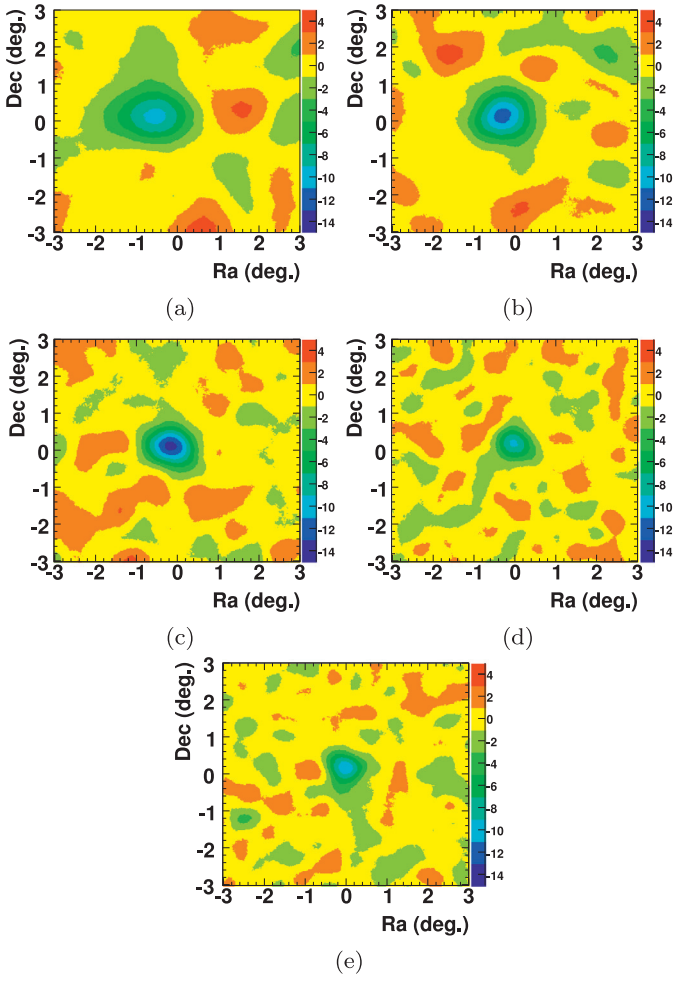

Fig. 2. Significance map observed with light moon data in five intervals of strip multiplicity, 400–600, 600–1000, 1000–2000, 2000–3000 and > 3000, from (a) to (e). The position of the moon is taken as the center of the coordinate system. The color scales show the level of significance of the deficit in terms of the standard deviation, i.e., σ.

Table 2
Event deficit in the on-source bin (ΔN), the number of events in the off-source bin (N_{off}), the optimal angular radius(ψ), and the statistical significance of the deficit.

N_{strips}	ΔN	N_{off}	ψ (°)	Significance (σ)
400–600	−1674	29,995	0.88	−9.8
600–1000	−2430	40,943	0.68	−12.1
1000–2000	−2964	46,561	0.56	−13.7
2000–3000	−1507	24,719	0.44	−9.8
≥ 3000	−1983	35,738	0.44	−10.5

N_{strips}. The deficit counts turns narrower with the increasing of N_{strips} because of the improvement of angular resolution. In the analysis these distributions are fit to a Gaussian function to estimate the position of the moon shadow. The mean of the Gaussian is regarded as the displacement of the moon in West-East direction. For the first two intervals, the fit range is taken in the interval $[-3°, 3°]$. The range is reduced to $[-1.5°, 1.5°]$ for the latter three cases. The fit parameters are shown in Table 3, the χ^2/ndf close to 1 simply means that a single Gaussian function is good to describe the distributions. The Gaussian fit neglects the asymmetry as result of geomagnetic field bending. For example in the worst case, as shown in the lowest interval of multiplicity we expect that the effect could lead to a 0.02° difference in the position, at the level of its error bar, this number becomes negligible as N_{strips} larger than

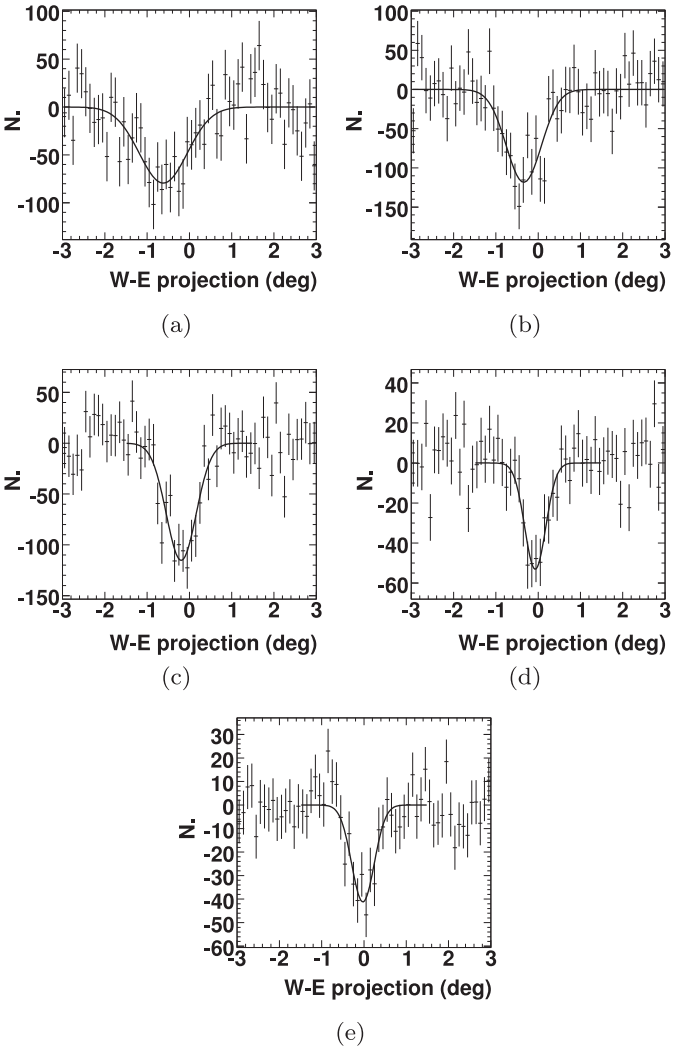

Fig. 3. Deficit event counts along West-East direction in the five intervals of strip multiplicity 400–600, 600–1000, 1000–2000, 2000–3000 and ≥ 3000, shown from (a) to (e), respectively.

Table 3
Fitted parameters in Fig 3 for the five intervals.

N_{strips}	χ^2/ndf	magnitude	mean (°)	sigma (°)
400–600	63.1/57	101. ± 15.	−0.58 ± 0.09	0.50 ± 0.10
600–1000	52.8/57	118. ± 13.	−0.34 ± 0.05	0.42 ± 0.05
1000–2000	30.2/27	115. ± 10.	−0.20 ± 0.04	0.35 ± 0.03
2000–3000	13.2/27	53. ± 7.	−0.07 ± 0.04	0.25 ± 0.04
≥ 3000	29.2/27	63. ± 8.	−0.05 ± 0.04	0.24 ± 0.03

1000. We also estimate the effect due to different fit ranges. By doubling the optimal radius (± 2Ψ), the change in the fit parameters is negligible.

6. Energy calibration and systematic uncertainty

6.1. Determination of the primary energy using the light Moon data

The observed displacement of the moon shadow as a function of the number of fired strips is shown in Fig. 4. In the same plot the expected displacement from the simulation is also shown. Horizontal and vertical error bars are the width of N_{strips} intervals and the error of the displacement, respectively. From the figure two important messages can be obtained:

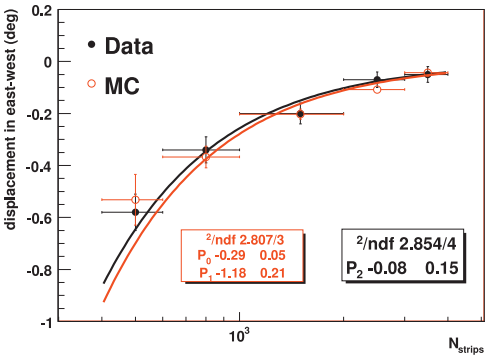

Fig. 4. Westward displacement of the moon shadow as function of the fired strips. The solid and open dots represent data and simulation, respectively. The black and red lines are the corresponding fit curves. (For interpretation of the references to colour in this figure legend, the reader is referred to the web version of this article.)

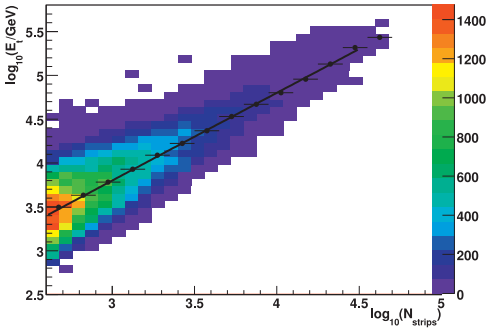

Fig. 5. Two dimensional histrogram for the measured N_{strips} and true energy E_t. The line represents the fit to the points using Eq. (1).

- Firstly, the data and the simulation are in good agreement within their errors. Both show an energy dependence as expected. Fig. 5 is a scatter plot between $N_{\rm strips}$ and true energy (E_t) in a log-log scale, the color profile represents the weight of the distribution. Based on the simulation data, a direct link can be constructed between $N_{\rm strips}$ and the energy. This link will provide an independent proof of the method for calibrating the energy scale of the experiment through the relation shown in Eq. (1). Here $E_{\rm r}$ represents the reconstructed energy in GeV and parameters k and λ depend on data selection criteria, $k = 0.81 \pm 0.03$ and $\lambda = 1.00 \pm 0.01$.

$$\log_{10}(E_{\rm r}) = k + \lambda \log_{10}(N_{\rm strips}). \quad (1)$$

- In order to quantify the difference between experimental data and simulation samples, the distribution of the simulated displacements is fitted using a function $p_0(\frac{N_{\rm strips}}{10^3})^{p_1}$ with parameters $p_0 = -0.30$ degree and $p_1 = -1.18$, shown as a red curve in Fig. 4. In the second step, experimental data are fitted with this standard function with a constant term multiplied on $N_{\rm strips}$ to take into account the difference between experimental data and simulation samples, i.e., $-0.30((1-p_2)(\frac{N_{strips}}{10^3}))^{-1.18}$ with $p_2 = -0.08 \pm 0.15$. The value of p_2 and its error is regarded as an estimator of the difference.

The energy resolution related to this reconstruction energy is defined as one standard deviation of the distribution of $\log(E_{\rm r}/E_{\rm t})$, where $E_{\rm t}$ is true energy input to the simulation. It is 0.27 as $E_{\rm r}$ is around 3 TeV, and better than 0.20 as $E_{\rm r}$ approaches to 10 TeV.

6.2. Systematic uncertainty of the calibrated energy

The systematic uncertainty of the energy is associated with the energy determination method. Four sources of the systematic un-

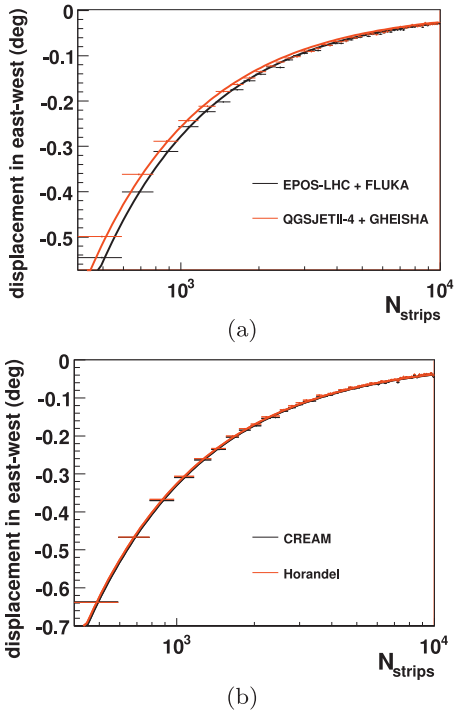

Fig. 6. (a) West-East displacement of the moon shadow as a function of N_{strips} from two different hadronic models. (b) Same distribution as (a) but for two different primary cosmic ray composition assumptions.

certainty are analyzed: geomagnetic field model, primary cosmic ray composition, hadronic interaction models and data selection cuts.

The simulations showed that more than 80% deviation for a cosmic ray particle induced by the geomagnetic field happened within the distance less than two radius of earth. Beyond five radius of earth, basically there is no deflection. That is to say, the geomagnetic field strengths near the surface play a important role in the studying. In the paper [28,29], at five different sites the measured field strengths has been compared with the model expectations, less than 1% difference was found. Considering about ARGO-YBJ detector's ability in angular resolution, this source uncertainty can be neglected in this analysis. In fact more sophisticated model, such as WMM2015 [30], is available to model the geomagnetic field, however considering about ARGO-YBJ detector angular resolution and intensive computation time, IGRF11 is a good model of the geomagnetic field.

A small dataset with QGSJET-II-4 [12] + GHEISHA [26] interaction models has been generated to estimate the systematic uncertainty caused by the high energy interaction models. The QGSJET-II-4 was selected because of its widely application in other experiments. The simulated displacement of the moon shadow in the West-East direction is shown in the top panel of Fig. 6. The relation between N_{strips} and the displacement from the QGSJET-II-4 + GHEISHA is analyzed in the same way, and compared to the results from the EPOS-LHC + FLUKA model, shown in Fig. 4. It yields a difference of 8% in the fitted parameter, which is therefore taken as the uncertainty from the hadronic models.

To evaluate the uncertainty from cosmic ray composition assumptions, the so-called Poly-gonato model [27] is adopted for comparison. The CREAM measurement indicates that the light component to full components ratio is around 65% in the region of 1–100 TeV, while the Poly-gonato model gives a ratio of approximately 62% in the same energy region. As shown in the bottom panel of Fig. 6, an overall westward shift difference of approximately 1% is observed for two models.

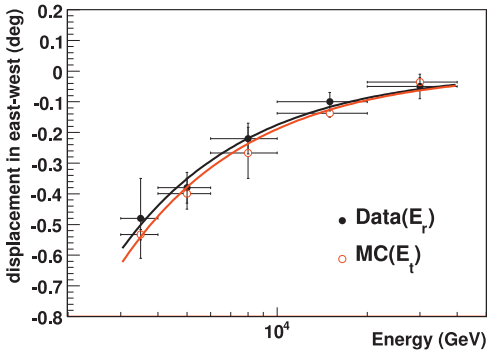

Fig. 7. Westward displacement of the moon shadow as function of the reconstructed energy, for MC samples the energy is true energy from the simulation. The solid and open dot represents experimental and simulation data, respectively; The black and red lines are the fitting curves to these two sets of dots. (For interpretation of the references to colour in this figure legend, the reader is referred to the web version of this article.)

The uncertainty from some data quality cuts is evaluated by slightly shifting the selection parameters within reasonable ranges, and then comparing the newly reconstructed energies with that obtained from the old ones. For the reconstructed core position, the selection cut is moved from 62 × 62 m^2 to 58 × 58 m^2. The value of maximum zenith angle of selected events is changed from 35° to 33°. Following the same procedure as described in previous chapters, the newly reconstructed energy is derived. The difference of the reconstructed energy between the two sets of data quality cuts is just 1.6% as N_{strips} is in range of 400–600, and around 2.5% as N_{strips} is higher than 3000.

In addition to the above uncertainties, the 2% uncertainty caused by the projection range is also taken into account. The total systematic uncertainty is then determined by quadratically adding the individual contributions and it is found to be around 16% for E_r in the energy range of 3–50 TeV.

7. Cross check using the reconstructed energy

7.1. Moon shadow westward shift using reconstructed energy intervals

The data sample is split into intervals of the reconstructed energy rather than that of strip, for the purpose of a careful cross check. Same LMD data samples are used, which are split in five energy intervals, namely 3–4, 4–6, 6–10, 10–20 and ≥ 20 TeV, and the same analysis method described in Section 6 is carried out. Deficits with −9.5, −9.9, −11.6, −11.7 and −10.1 s.d. are correspondingly obtained . The westward displacement of the moon shadow is compared for data and simulation as shown in Fig. 7. They agree within their systematic uncertainties. We regard this as a proof of the fact that the reconstructed energy calibrated with the Moon shadow is a solid energy estimator.

7.2. Comparison to light component cosmic ray energy spectrum

As a further cross-check, the differential energy spectrum of light components (proton + Helium) are measured using the same dataset but with opening angle less than two degrees relative to moon direction along the moon's orbit. To match a general cut on zenith angle (cut 2), the zenith angle of the moon is required to be less than 30°. The differential spectrum is calculated according to its standard definition, $J(E) = \phi_0 E^{-\gamma} = \frac{\Delta N}{\Delta E A_{\rm eff} \Omega T}$ where T is the total live-time, Ω is the solid angle relative to 2 degree; $A_{\rm eff}$ is the effective collection area, which could be determined from the simulation $A_{\rm eff} = \frac{\Delta N_{\rm rec}}{\Delta N_{\rm gen}} A_{\rm gen} \frac{\cos(\theta_{\rm max}) + \cos(\theta_{\rm min})}{2}$ where $N_{\rm gen}$ is the

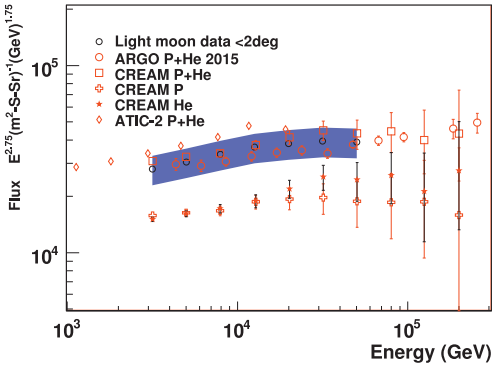

Fig. 8. Differential energy spectrum of the light component measured with the ARGO-YBJ light moon data, compared with other measurements, CREAM, ATIC and ARGO-YBJ unfold technique [8,9,25].

Table 4
Values of measured light cosmic ray spectrum. Energy range is in the unit of $log_{10}(E/GeV)$, the flux unit is $m^{-2}s^{-1}sr^{-1}GeV^{-1}$.

Energy range	Flux ± stat. error	$N^{moon}_{deficit}$	$N^{moon}_{expected}$
3.4 – 3.6	$(6.63 \pm 0.02) \times 10^{-6}$	1276 ± 102	1319 ± 36
3.6 – 3.8	$(2.04 \pm 0.03) \times 10^{-6}$	968 ± 53	911 ± 30
3.8 – 4.0	$(6.31 \pm 0.03) \times 10^{-7}$	647 ± 46	594 ± 24
4.0 – 4.2	$(1.94 \pm 0.01) \times 10^{-7}$	409 ± 23	378 ± 19
4.2 – 4.4	$(5.72 \pm 0.05) \times 10^{-8}$	217 ± 24	227 ± 15
4.4 – 4.6	$(1.67 \pm 0.02) \times 10^{-8}$	146 ± 16	130 ± 11
4.6 – 4.8	$(4.63 \pm 0.07) \times 10^{-9}$	79 ± 11	70 ± 8

number of generated showers with the core position distributed over a large area A_{gen}, $\theta_{min} = 0^\circ$, $\theta_{max} = 40^\circ$. After applying the above analysis procedure, N_{rec} events were survived after the trigger conditions, the reconstruction cuts and other data selections cuts. By assuming the chemical composition measured by CREAM, Fig. 8 shows the final proton + Helium spectrum from 2.5 TeV to 50 TeV with an energy bin of $\Delta \log_{10}(E) = 0.2$. From Fig. 7 the calibrated energy with moon shadow is less than 30 TeV. To compare with other results, here a little extrapolation has been conducted to reach energy of 50 TeV. The measured values along with their uncertainties (statistical only) are listed in Table 4. A power-law fit has been performed, and compared to the light spectrum from ARGO-YBJ measurement (with unfolding method) and the CREAM experiment. The value of the spectrum slope is 2.63 ± 0.01, which agrees quite well with $\gamma^{unfold}_{argo} = 2.64 \pm 0.01$ and $\gamma_{cream} = 2.62 \pm 0.02$. As to the flux intensity, this calibrated spectrum agree well with that of the CREAM and ARGO-YBJ unfolding measurement within their errors.

In the flux estimation, the effect of the contamination of heavier primaries has also been estimated. The fraction of nonlight elements passing through the event selection is calculated, based on the simulation samples using the Fluka+SIBYLL according to nonlight contribution from Horandel model. In the energy range of 1–100 TeV, this ratio is 2.4%. In the energy region below 50 TeV, the highest differential contribution does not exceed 11%. The measured flux has been corrected by this amount. Thus no additional contribution caused by heavier primaries is then added.

Furthermore, in the flux calculation our treatment ignores the effect caused by the moon shadow. Since the opening angle is two degrees and eight times larger than the angular radius of the moon, we expect that it should influence the result in the 1.6% percent level. $N^{moon}_{expected}$ in Table 4 is the expected events from the Moon, $N^{moon}_{deficit}$ is the deficit events from moon shadow measurement. A good agreement between $N^{moon}_{deficit}$ and $N^{moon}_{expected}$ shows the consideration about the moon shadow is quite reasonable.

The shaded area in Fig. 8 represents the systematic uncertainties, where three main contributions have been included: the opening angle around moon center, selection cut efficiencies and the uncertainty in the energy determination:

- A different cut of the opening angle has been used to estimate the contribution from this cut. An opening angle of 4° around the moon center yields a difference smaller than 1%. Thus the contribution in flux intensity from this cut is less than 1%.
- The differences in the effects of quality cuts described in Section 4 as applied to experimental data and MC samples lead to a systematic uncertainty on the efficiency listed in Table 1. A difference around 5.8% is included on the systematic uncertainty on the flux estimation.
- A systematic uncertainty on the reconstructed energy will change into a systematic shift of the total flux, as discussed in Section 6.1. It is at the level of 16%.

The total systematic uncertainty is determined by adding the individual contributions quadratically. The total systematic uncertainty was found to be around 17% in energy range of 3–50 TeV and shown as shaded area in Fig. 8.

8. Conclusion and outlook

In this work, the data from the direction around the moon is analyzed after carefully selecting light primary cosmic ray compositions. The moon shadow has been detected with the highest significance up to 13.7σ. Using primary particles transported through Earth-Moon spectrometer system, the detector energy scale, i.e., the relation between the energy and the number of fired strips is calibrated. The resolution of the reconstructed energy is around 27% around 3 TeV, and it turns to be 20% as energy is higher than 10 TeV. The result shows that the reconstructed energy of MC simulation and experimental data, tuned by moon shadow data, is consistent with each other within 16–18% level. As a further cross-check, the light component differential spectrum has been derived using the calibrated moon light data, from 3 TeV to 50 TeV. The results are compatible regarding either the slope of spectrum or the absolute flux with the spectrum obtained by ARGO-YBJ unfolding technique. All these results can be seen as an experimental verification of this energy scale.

This way of calibrating energy can be used for future experiments, such as LHAASO (Large High Altitude Air Shower Observatory), where disentangling the charge dependence on the energy determination of primary nuclei is also a problem. Once the moon shadow induced by a kind of cosmic ray component is observed, the deflection of the shadow position can be used to tune the reconstructed energies.

Acknowledgments

This work is supported in China by NSFC (10120130794), the Chinese Ministry of Science and Technology, the Chinese Academy of Sciences, the Key Laboratory of Particle Astrophysics, CAS, and in Italy by the Istituto Nazionale di Fisica Nucleare (INFN).

We also acknowledge the essential supports of W.Y. Chen, G. Yang, X.F. Yuan, C.Y. Zhao, R. Assiro, B. Biondo, S. Bricola, F. Budano, A. Corvaglia, B.D Aquino, R. Esposito, A. Innocente, A. Mangano, E. Pastori, C. Pinto, E. Reali, F. Taurino and A. Zerbini, in the installation, debugging and maintenance of the detector.

References

[1] G.W. Clark, Phys. Rev. D 108 (1957) 450.
[2] D.E. Alexandreas, et al., Phys. Rev. D 43 (1991) 1735.
[3] M.G. Aartsen, et al., Icecube collaboration, Phys. Rev. D 89 (2014) 102004.
[4] R. Caballero, et al., MINOS observation of shadowing in the muon flux underground, merida, ICRC Proc. (2007).
[5] B. Bartoli, et al., ARGO-YBJ collaboration, Phys. Rev. D 85 (2012) 022002.
[6] M. Amenomori, et al., AS-gamma collaboration, ApJ 692 (2009) 61.

[7] G. Aielli, et al., ARGO-YBJ collaboration, Phys. Rev. D 84 (2011) 022003.
[8] A.D. Panov, et al., Bull. Russ. Acad. Sci. Phys. 73 (2009) 564.
[9] Y.S. Yoon, et al., ApJ 728 (2011) 122.
[10] H.S. Ahn, et al., ApJ 707 (2009) 593.
[11] O. Adriani, et al., Science 1199172 (2011).
[12] S.S. Ostapchenko, Phys. Rev. D 83 (2011) 014018.
[13] G. Aielli, et al., ARGO-YBJ collaboration, NIMA 562 (2006) 92.
[14] A. Aloisio, et al., ARGO-YBJ collaboration, IEEE Trans. Nucl. Sci. 51 (2004) 1835.
[15] C.C. Ginlay, S. Maus, C.D. Beggan, International geomagnetic reference field: the eleventh generation, Geophys. J. Int. 183 (2010) 1216.
[16] D. Heck, J. Knapp, J. Capdevielle, G. Schata, T. Thouw, CORSIKA: A monte carlo code to simulate extensive air showers, Report FZKA 6019 (1998).
[17] G. Battistoni, et al., AIP Conference Proceedings 896 (2007) 31.
[18] T. Pierog, et al., Phys. Rev. C 92 (2015) 034906.
[19] G. Yi-Qing, et al., CPC(HEP & NP) 34 (2010) 555.
[20] J. Allison, et al., IEEE Trans. Nucl. Sci. 53 (2006) 270.
[21] G. Aielli, et al., ARGO-.YBJ collaboration, Phys. Rev. D 80 (2009) 092004.
[22] M. Zha, Nuclear Physics B (Proc. Suppl.) 175+176 (2008) 443.
[23] R. Fleysher, L. Fleysher, P.A.I. Mincer, ApJ 603 (2004) 355.
[24] L. TiPei, M. YuQian, ApJ 272 (1983) 317.
[25] B. Bartoli, et al., ARGO-YBJ collaboration, Phys. Rev. D 91 (2015) 112017.
[26] H. Fesefeldt, Report PITHA-85/02 (1985). RWTH Aachen, available from: http://cds.cern.ch/record/162911/files/CM-P00055931.pdf
[27] J.R. Horandel, Astropart. Phys. 19 (2003) 193.
[28] A. Chulliat, E. Thebault, Earth Planets Space, 62 (2010) 805.
[29] L. Yuanyuan, et al., Acta Seismol. Sin. 35 (2013) 125.
[30] A.S. Macmillan, et al., The US/UK world magnetic model for 2015–2020, in: NOAA National Geophysical Data Center, Boulder, CO, 35, 2013, p. 125, doi:10.7289/V5TH8JNW.